


Cite this: *RSC Adv.*, 2019, 9, 31645

Adsorption performance of antimony by modified iron powder

Chun Zhang, * Haiyan Jiang, Yumei Deng and Aihe Wang

Antimony pollution resulting from industrial production is a great threat to the environment, ecology and the human body. Zero-valent iron powder is low-cost and easy to obtain. Nevertheless, the lower adsorption capacity limits its application when it is used as an adsorbent. In the present study, ball-milling and acid modification were developed to change its surface characteristics and γ -Fe₂O₃, γ -FeOOH and Fe₃O₄ were obtained after treatment, which promoted its adsorption capacity. Compared with the raw iron powder, the adsorption capacities for Sb(III) and Sb(V) using the modified material were increased from 12.93 mg g⁻¹ and 5.47 mg g⁻¹ to 17.96 mg g⁻¹ and 10.58 mg g⁻¹, respectively. The study showed that the experimental data fitted the Langmuir model and the pseudo-first-order kinetic model better; the adsorption process was monolayer and chemically controlled at pH 5.0 \pm 0.2. XPS and FT-IR analysis showed that Fe–O–Sb bonds arose during the adsorption process. The effect of pH on the adsorption capacity was also studied and the pH affected the adsorption of Sb(V) more than the adsorption of Sb(III). In addition, the modified iron powder presented better efficiency when applied to the removal of low levels of antimony in drinking water. Based on the increase of adsorption capacity and low cost, iron powder should be a promising adsorbent for aqueous antimony removal.

Received 23rd July 2019
Accepted 13th September 2019

DOI: 10.1039/c9ra05646g

rsc.li/rsc-advances

1 Introduction

Antimony was widely used as an industrial additive in past decades in various industrial production processes, such as flame retardancy, in bearing and gear production, for corrosion-resistant chemical pipes, in rubber, in gasoline, as a catalyst for organic synthesis and even in ammunition production and so on.^{1,2} Because of its carcinogenicity and as a cumulative heavy metal, the wide application of antimony also brought serious environmental problems. Because of its high toxicity, antimony and its compounds have been classified as the pollutants for priority control by the Environmental Protection Agency of United States (US EPA) and the European Environment Agency (EEA) and the maximum contaminant concentration is strictly set as 6 μ g L⁻¹ in drinking water by the US EPA and as 5 μ g L⁻¹ by the EEA.^{3,4}

As the largest antimony producer in the world, 90% of the antimony in the world comes from China; the vast majority of antimony in China was produced in the Lengshuijiang Xikuang area in Hunan province, which is known as ‘the antimony capital of the world’.⁵ The soil, plants and the Zijiang River near the Xikuang deposits are under the threat of serious antimony pollution caused by antimony mining and processing. In November 2015, the leakage of more than 3000 tons of tailings

containing antimony in the Longxing Antimony Industry Co. Ltd., in Gansu province in China resulted in excessive amounts of antimony in more than 300 km of the Jialing River and the western Han River. The leakage event involved Gansu, Shanxi and Sichuan provinces and brought great threat to the safety of the drinking water and the ecological system.^{6,7} After diffusion into the ecological environment, it is difficult for antimony to be enriched; the antimony contaminated soil and water resources may cause great harm to the human body through the food chain. Consequently, it is necessary to develop efficient technologies to treat antimony containing wastes to reduce the antimony pollution factor from the emission source.

Antimony has two valence states, trivalent antimony (Sb(III)) and pentavalent antimony (Sb(V)). The Sb(III) has more toxicity than Sb(V) and can be oxidized into Sb(V) in oxidizing atmospheres. The occurrence of the Sb(V) species is ranked as SbO₂⁻ at pHs below 2, H₂SbO₄ at pH 2 and 2.7, H₂SbO₄⁻ and Sb(OH)₆⁻ at pH 2.7 and 10.4.⁷ Antimony containing wastewater is one of the most important wastes in the process of antimony production. Presently, adsorption, electrochemical methods, biological methods, co-precipitation and coagulation-precipitation are generally used to treat antimony containing waste water.³ Considering the cost, its application and the secondary pollution, adsorption has been considered as an attractive method because it has been proved to be efficient, cost-effective and simple to perform compared to other methods.^{3,8} Nevertheless, the core part of the adsorption techniques is the adsorption material, which is the key factor of the treatment.

School of Municipal and Mapping Engineering, Hunan City University, Yiyang 413000, China. E-mail: zhangchun7912@163.com; Fax: +86 737 4628718; Tel: +86 737 4628718

As reported, iron oxides have strong binding for antimony and multiple iron oxides have been demonstrated to be effective for Sb removal. Both Sb(III) and Sb(V) appear to be adsorbed strongly to iron oxides, and thereby greatly affect the speciation, mobility and the fate in the environment. The iron oxide minerals, including the hydrous ferric oxides: goethite, akageneite, lepidocrocite, and hematite showed favourable affinity for Sb(III) and Sb(V). Additionally, some magnetic iron oxides and metal-doped ferrites were synthesized to remove the antimony in wastewater.^{9,10} Previous researchers synthesized validated iron oxy-hydroxide (FeOOH) and amorphous Fe₃O₄/FeOOH nanocomposite for the removal of Sb(III) and Sb(V) from drinking water with an Sb level below the regulation limit of 5 µg L⁻¹. In recent years, the zero-valent iron (Fe⁰) has drawn increasing attention as an effective remediation medium for many contaminants and was considered to be promising and cost-effective. Whereas, the zero-valent iron nanoparticles generally present high agglomeration and lack chemical stability.^{12,13}

In this research, the granulated zero-valent iron powders were adopted as a new adsorbent and then they were activated and stabilized using acetic acid. The physicochemical characteristics of the modified and activated iron powders were determined by the particle size, XRD and SEM analyses. Additionally, the characteristics of the antimony adsorption process and the antimony removal mechanisms by the granular adsorbent were determined using a combination of XRD, XPS and FT-IR observations and the probable schematic process diagram for the adsorption process was developed.

2 Materials and methods

2.1 Materials

All the chemical reagents used in this study were of analytical grade and were purchased from Sinopharm Chemical Reagent Beijing Co., Ltd., and used without further purification. All the solutions used were prepared using deionized water. The weighed K₂H₂Sb₂O₇·4H₂O was dissolved in 1 L of deionized water to prepare the Sb(V)-containing solution and Sb₂O₃(III) was dissolved using 2.0 mol L⁻¹ HCl. It should be noted that Sb(III) in all figures in this paper represents uncomplexed-Sb(III) for simplification.

2.2 Sample preparation and characterization

The iron powders adopted in the experiments were obtained from the pharmaceutical group, China. The stainless-steel balls were used as the ball grinding medium. After grinding for two hours, the sample was collected and the particle size change was determined. Then, the ground iron powders were immersed in acetic acid solution with a pH of 5.0 and mixed for 24 hours at a speed of 160 rpm. After filtration using a 0.45 µm membrane, the immersed iron powders were collected and dried in a vacuum drying oven and characterized, and were then ready for the following batch experiments.

2.3 Batch adsorption experiments

2.3.1 Adsorption isotherm. The adsorption isotherms and kinetics for Sb(III) and Sb(V) on the activated and modified iron

powder granules at 25 °C were determined using Sb(III) and Sb(V) containing solutions with initial concentrations from 0 to 20 mg L⁻¹. The adsorbent dose was 0.5 g L⁻¹ at a pH of 5.0 ± 0.2 and the reaction time was 360 min. The pH of the solution was regulated using 0.01 mol L⁻¹ HCl and NaOH. After the solid-liquid separation, the concentrations in the remaining solution were determined using an ICP method. Then, the experimental data were fitted according to the Langmuir and the Freundlich models and the relative constants were calculated.

2.3.2 Adsorption kinetics. The effect of reaction time on the adsorption of Sb(III) and Sb(V) by the materials were measured in a series of 100 mL polythene centrifuge tubes for 1, 2, 4, 6, 8, 10 and 12 h. The temperature was set at 25 ± 1 °C, the adsorbent dose used was 0.5 g L⁻¹ and the pH was 5 ± 0.2. The initial Sb concentration was determined to be 20 mg L⁻¹. After the reaction, the mixture was separated and the solution was analyzed to determine residual antimony concentration and the kinetic characteristics using the pseudo-first-order kinetic model and the pseudo-second-order kinetic model.

2.3.3 Effect of pH. The effects of pH on the adsorption capacity of Sb(III) and Sb(V) by the modified material were determined. The reaction temperature was set at 25 ± 1 °C. The initial Sb(III) and Sb(V) concentrations were both determined to be 20 mg L⁻¹. The adsorbent dose was 0.25 g L⁻¹ and the experimental pH range was between 3 and 10. The total reaction time was 360 min. The effect mechanism was also determined.

2.3.4 Application for the removal of low-levels of antimony in a water source. The application prospects of the modified iron powder in the removal of low-levels of antimony in a water source were also studied. The reaction temperature was also set at 25 ± 1 °C and the adsorbent dose was 0.25 g L⁻¹; the pH of the solution was set at 7.0 ± 0.2 and the total solution volume was 100 mL. The total reaction time was 360 min and all the experiments were completed three times in parallel and the experimental errors were within 5%.

2.4 Analytical methods

The residual Sb(III) or Sb(V) concentrations in the solutions were determined by ICP-AES (VG PQ ExCell, Thermo Electron Corporation). The pH of the solutions was measured using a pH meter (PHS-3B, Jingke, Shanghai, China). The X-ray diffraction patterns of the material were recorded using an X-ray diffractometer (D8 Discover, Bruker) with Cu Kα radiation (40 kV, 40 mA). The SEM, and FT-IR analyses were completed using scanning electron microscopy (Tecnai G2, FEI), and the Fourier-Transform Infrared Spectrometry (Nicolet iS10, Nicolet), respectively. The X-ray photoelectron spectroscopy (XPS) spectra were obtained with an XPS analyzer (ESCALAB250Xi, Thermo-Fisher) with an Al Kα X-ray source (power: 200 W).

3 Results and discussion

3.1 Material characterization

The differential particle size distribution of the raw and the ground iron powders are presented in Fig. 1. The average particle size was reduced from about -105 µm to -50 µm after



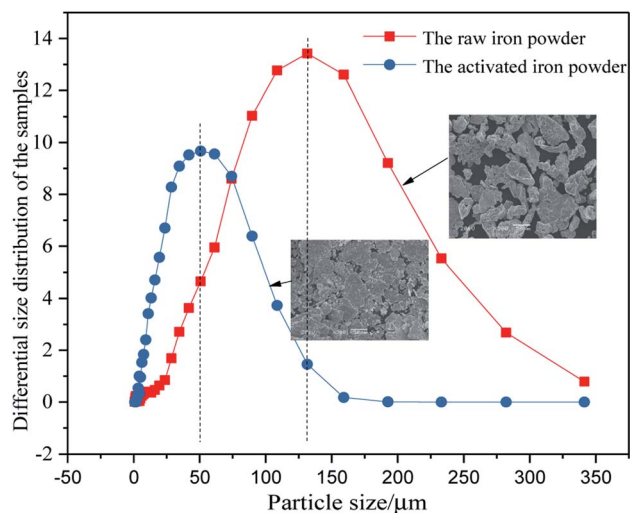


Fig. 1 Changes in the particle size distribution of the raw and the ground iron powders.

the raw iron powders were milled. As Fig. 1 shows, the largest particle size between 108.61 μm and 131.47 μm was obtained for 13.42% of the total particles before ball-milling treatment. Accordingly, the largest size between 41.84 μm and 50.64 μm was obtained for 9.67% of the total particles after ball-milling treatment. The ground iron powders were immersed in the acetic acid solution with pH of 5.0 and mixed for 24 hours. The iron powders with a smaller particle size possessed a more

active physical chemistry, which led to the faster formation of the corrosion layer. Then, the immersed iron powders were dried in a vacuum drying oven and characterized. The results are presented in Fig. 2. The surface of the activated and modified iron powders became rough, as shown in Fig. 2(b) and (d), when compared with Fig. 2(a), which implied that new phases had been obtained. The ground iron powders are presented in Fig. 2(d) and the corrosive ground iron powders are shown in Fig. 2(e). The X-ray diffraction analysis of the samples in Fig. 2(f) showed that the diffraction peaks of Fe_3O_4 , $\gamma\text{-Fe}_2\text{O}_3$ and $\gamma\text{-FeOOH}$ appeared, which implied that the physicochemical property of the treated iron powder had changed greatly.

3.2 Adsorption isotherm

The relationship between the equilibrium concentration of Sb(III) and Sb(V) in the solution and the loading on the adsorbents is presented in Fig. 3(A). The experimental data fitted was based on the Langmuir and the Freundlich models. The linearized forms of the Langmuir and Freundlich equations of $C_e/q_e \sim C_e$ and $\log q_e \sim \log C_e$ are shown in Fig. 3(B) and (C), respectively. The Langmuir isotherm model is described according to the following expression:

$$q_e = \frac{q_m K_L C_e}{1 + K_L C_e} \quad (1)$$

where q_m is the maximum adsorption capacity (mg g^{-1}); K_L is the constant for the Langmuir model (L mg^{-1}); q_e is the

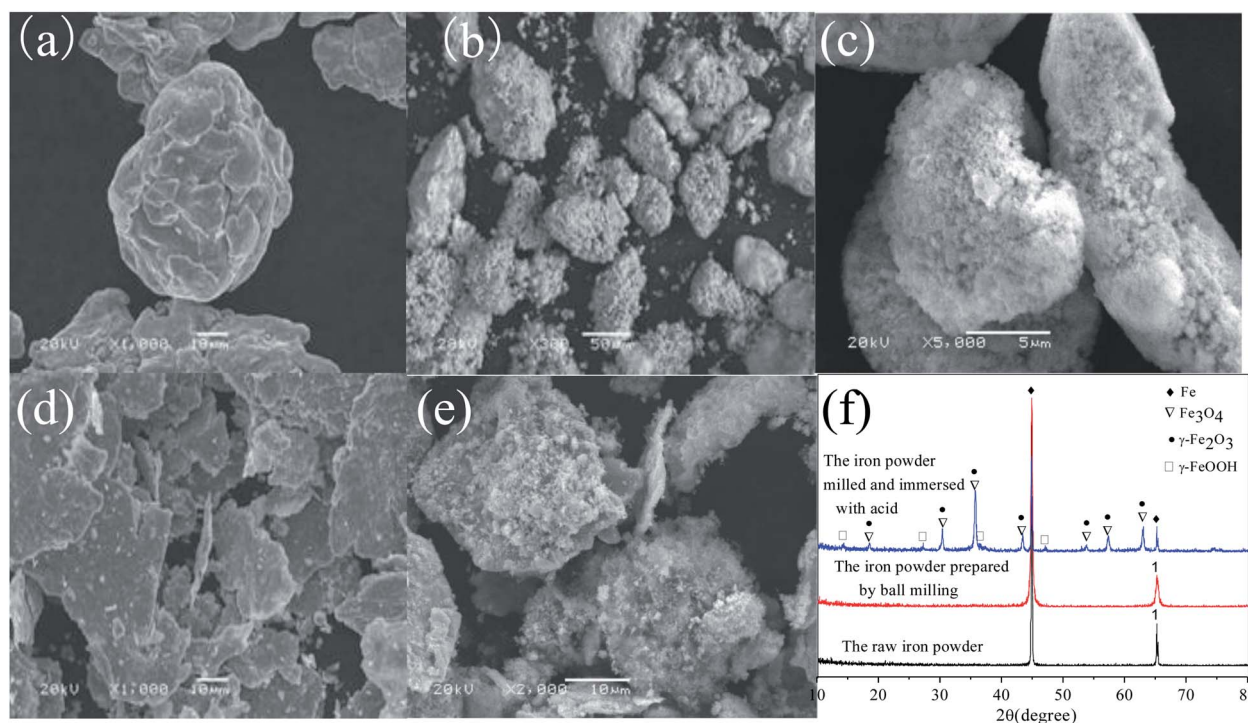
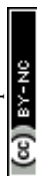


Fig. 2 Changes in the physicochemical properties of the raw and the treated iron powders: (a) the raw iron powders; (b and c) the corrosive iron powders; (d) the ground iron powders; (e) the ground iron powder after corrosion; (f) and the XRD analysis of the ground and corrosive iron powders.



equilibrium content in the adsorbent (mg g^{-1}); C_e is the equilibrium concentration of the adsorbate in the solution (mg L^{-1}).

The nonlinear Langmuir isotherm expression can be converted into the following linear model:

$$\frac{C_e}{q_e} = \frac{1}{q_m K_a} + \frac{C_e}{q_m} \quad (2)$$

The Freundlich isotherm model is an empirical equation used to express adsorption on a heterogeneous surface; the nonlinear and linear expressions are shown in eqn (3) and (4), respectively:

$$q_e = K_F C_e^{1/n} \quad (3)$$

$$\log q_e = \frac{1}{n} \log C_e + \log K_F \quad (4)$$

where q_e and C_e are identical to those in the Langmuir model shown previously; K_F is the Freundlich constant (mg g^{-1}); n is a constant implying the adsorption intensity or surface heterogeneity.

The adsorption isotherms for Sb(III) and Sb(V) and the fitting results are presented in Fig. 3. The related parameters of the

adsorption process and maximum adsorption capacity were estimated according to the fitted linear equations of the Langmuir and Freundlich model and are presented in the Table 1. Just as the Table 1 showed, the correlation coefficients for the Langmuir model ($0.9871 < R^2 < 0.9978$) were higher than the correlation coefficients for the Freundlich model ($0.9184 < R^2 < 0.9873$). The correlation coefficients for all the adsorption cases revealed that the Langmuir model fitted the adsorption of Sb(III) and Sb(V) better than the Freundlich model based on the higher correlation coefficients. The Langmuir model is based on the theory of monolayer adsorption on a uniform surface and the adsorption ability of the adsorption sites is uniform.^{2,14}

The uptake of the adsorbate only happens on the surface of the adsorbent. The maximum adsorption capacities of the modified iron powders for Sb(III) and Sb(V) were 17.96 mg g^{-1} and 10.58 mg g^{-1} , respectively, which was greatly elevated compared with adsorption of the raw iron powders. However, the adsorption capacities for Sb(III) and Sb(V) were still below the values reported in the previous reports.^{2,14} The lower maximum adsorption capacity was because the iron oxides just occurred on the surface of the iron powders, but the completely synthesized iron oxides were adopted in the study. The value of K_a of the modified iron powders for Sb(III) was higher than that for Sb(V), which implied that there was a larger

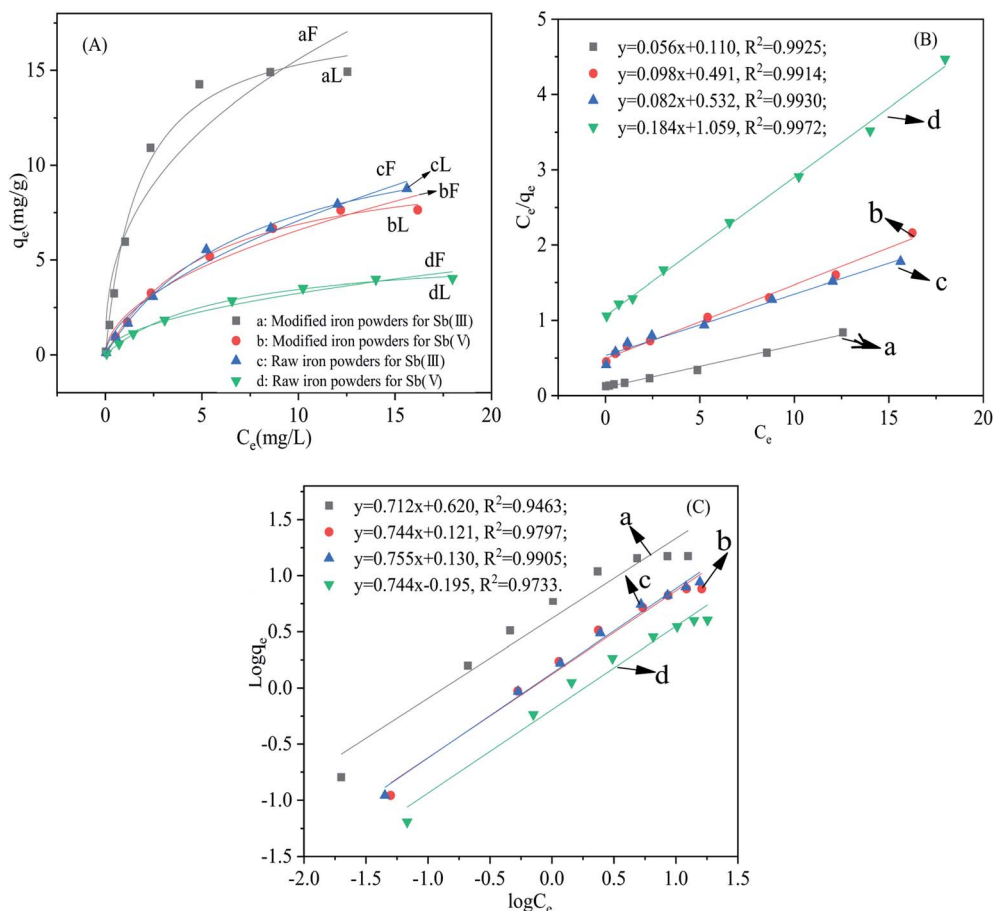
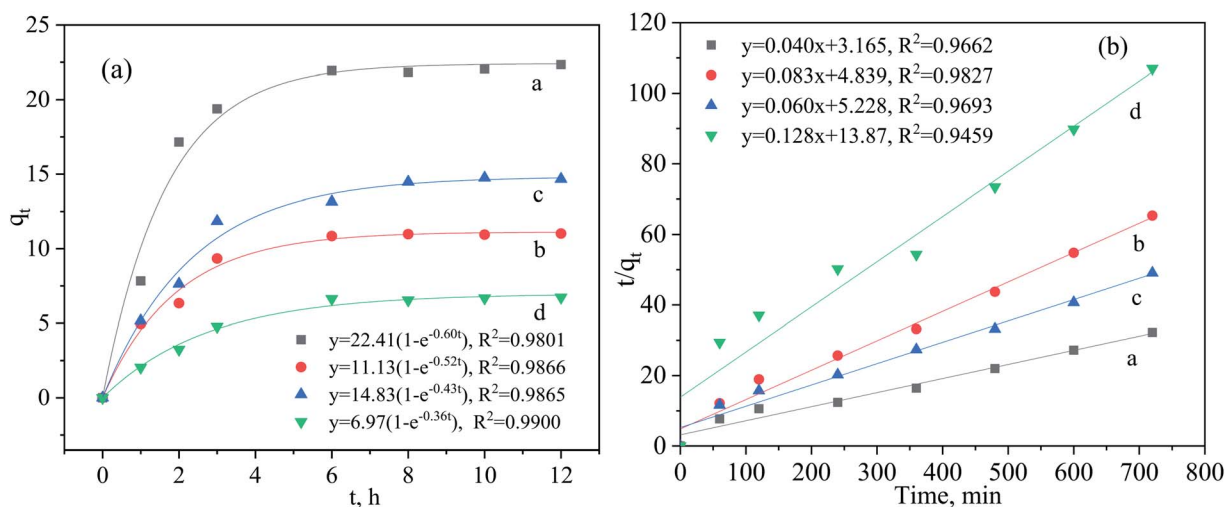


Fig. 3 Adsorption isotherms for Sb(III) and Sb(V): (A) the Langmuir and Freundlich fitting analysis; (B) the linear Langmuir $C_e/q_e \sim C_e$ analysis; and (C) The linear Freundlich $\log q_e \sim \log C_e$ analysis ($t = 25 \pm 1^\circ \text{C}$; adsorbent dose: 0.5 g L^{-1} ; $\text{pH} = 5 \pm 0.2$; reaction time: 360 min).



Table 1 Parameters of the Langmuir and Freundlich models for the adsorption of Sb(III) and Sb(V)

Material type	Equation Parameter	Langmuir ($q_e = \frac{q_m K_L C_e}{1 + K_L C_e}$)			Freundlich ($q_e = K_F C_e^{1/n}$)		
		q_m (mg g ⁻¹)	K_L (L mg ⁻¹)	R^2	K_F (mg g ⁻¹)	n	R^2
The modified iron powders	Sb(III)	17.96	0.57	0.9871	6.27	2.53	0.9184
The modified iron powders	Sb(V)	10.58	0.18	0.9960	2.01	1.92	0.9731
The raw iron powders	Sb(III)	12.93	0.13	0.9981	1.87	1.73	0.9873
The raw iron powders	Sb(V)	5.47	0.17	0.9978	1.01	1.98	0.9782

**Fig. 4** Adsorption kinetics of Sb(III) and Sb(V): (a) the non-linear pseudo-first-order kinetic model analysis; and (b) the linear pseudo-second-order kinetic model analysis ($t = 25 \pm 1^\circ\text{C}$; adsorbent dose: 0.5 g L^{-1} ; pH = 5 ± 0.2 ; initial Sb concentration: 20 mg L^{-1} ; time range: 0–720 min).

affinity for Sb(III) than Sb(V) on the adsorbent. Although the correlation coefficient for the Freundlich model was smaller than that of the Langmuir model, the value of K_F for the adsorption process using the modified iron powders was higher than that of the raw material, which showed a higher adsorption and bonding affinity.^{14,15}

3.3 Adsorption kinetics

Based on the previous experiments, it was clear that the adsorption capacity of the modified iron powders increased dramatically compared with the raw iron powders. Moreover, the adsorption kinetics were always used to assess the adsorption efficiency of Sb(III) and Sb(V) by the raw and the modified iron powders. In this study, the pseudo-first-order kinetic

model, the pseudo-second-order kinetic model and the intra-particle diffusion were used to complete the relative calculation.^{2,16}

The non-linear pseudo-first-order kinetic model is expressed as follows:

$$q_t = q_e(1 - e^{-k_1 t}) \quad (5)$$

The above non-linear expression can be converted into the following linear form:

$$\log(q_e - q_t) = \log q_e - \frac{k_1}{2.303} t \quad (6)$$

Table 2 Adsorption kinetics constants for the adsorption of Sb(III) and Sb(V)

Material type	Pseudo-first-order kinetic model			Pseudo-second-order kinetic model		
	k_1 (h ⁻¹)	q_e (mg g ⁻¹)	R^2	k_2 (g mg min ⁻¹)	q_e (mg g ⁻¹)	R^2
Modified iron powders for Sb(III)	0.60	22.41	0.9801	0.51×10^{-3}	25.00	0.9662
Modified iron powders for Sb(V)	0.52	11.13	0.9866	1.42×10^{-3}	12.05	0.9827
Raw iron powders for Sb(III)	0.43	14.83	0.9865	0.69×10^{-3}	16.67	0.9693
Raw iron powders for Sb(V)	0.36	6.97	0.9900	1.18×10^{-3}	7.81	0.9459



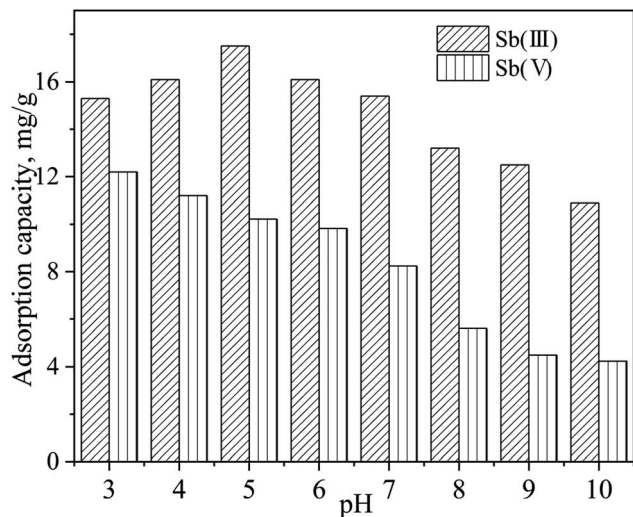


Fig. 5 Effect of pH on the adsorption capacities for Sb(III) and Sb(V) of the modified iron powders ($t = 25 \pm 1$ °C; initial Sb(III) and Sb(V) concentration: 20 mg L^{-1} ; total solution volume: 250 mL ; adsorbent dose: 0.25 g L^{-1} ; pH range: 3–10; reaction time: 360 min).

The pseudo-second-order kinetic model is expressed as follows:

$$q_t = \frac{q_e^2 k_2 t}{1 + q_e k_2 t} \quad (7)$$

The corresponding linear form is as follows:

$$\frac{t}{q_t} = \frac{1}{k_2 q_e^2} + \frac{1}{q_e} t \quad (8)$$

where q_t (mg g^{-1}) is the adsorption capacity at time t (min); q_e (mg g^{-1}) is the adsorption amount at equilibrium; k_1 (min^{-1})

and k_2 ($\text{g mg}^{-1} \text{ min}^{-1}$) are the equilibrium constants for the pseudo-first and pseudo-second order reactions, respectively.

The effect of the reaction time on the adsorption capacity (q_t) of Sb(III) and Sb(V) at time t by the modified and the raw iron powders are presented in Fig. 4. The non-linear pseudo-first-order kinetic model and the linear pseudo-second-order kinetic model were adopted to fit the adsorption data.^{4,9} According to the results shown in Fig. 4(a), the uptake of Sb on the adsorbents increased greatly in the first two hours, which was always attributed to the adsorption by the high affinity sites or the precipitation of adsorbate on the surface of the adsorbent. About 85% uptake of Sb(III) on the adsorbent occurred in the first three hours and in the following stage, intraparticle diffusion may dominate the adsorption process and the adsorption reached equilibrium after reaction for 6 h. As shown in Table 2, the calculated q_e , resulting from the pseudo-first-order kinetic model, was approximately equal to that from the Langmuir isotherm model and the reaction process was monolayer adsorption and was controlled by the chemical reaction, which was also demonstrated by the results of the XPS and FT-IR analyses. Although the maximum adsorption capacities of the modified iron powders for Sb(III) and Sb(V) obtained in this study were relatively lower than those for the pure α -FeOOH, α -Fe₂O₃ and metal doped Fe₃O₄,^{9,14} the adsorbent (the modified iron powders) in present study can be easily obtained and the method is financially feasible, which could be the greatest advantage of using this material.

3.4 Effect of pH on the adsorption process

The effects of the initial solution pH (from 3 to 10) on the removal of Sb(III) and Sb(V) by the modified iron powders were determined and the results are presented in Fig. 5. According to the results in Fig. 5, the adsorption capacity was reduced from 15.3 mg g^{-1} to 10.9 mg g^{-1} for Sb(III) and from 12.2 mg g^{-1} to 4.24 mg g^{-1} for Sb(V). The initial solution pH affected the removal of Sb(III) slightly. However, the adsorption capacity of Sb(V) decreased greatly with the increase of pH from 3 to 10. Results in previous reports showed that the adsorption process of Sb(III) by hydroxyapatite (at pHs between 5 and 10) and by goethite (at pHs between 2 and 12) was not greatly influenced by the initial solution pH.^{13,17} The adsorption behavior can also be explained by the values of the points of zero charge. As previously reported, the zero charge of γ -Fe₂O₃, γ -FeOOH and Fe₃O₄ were 8.6, 7.3 and 4.5, respectively.^{2,16} Below the value of the zero charge, the surface of the iron oxides can be protonated according to the reaction: $\equiv\text{FeOH} + \text{H}^+ \leftrightarrow \equiv\text{Fe-OH}_2^+$; the protonated form can also promote electrostatic adsorption of Sb anionic species (H_2SbO_3^- , $\text{Sb}(\text{OH})_4^-$, H_2SbO_4^- , $\text{Sb}(\text{OH})_6^-$).¹⁰ However, above the value of the zero charge, the surface of the iron oxides on the corrosion layer could be coated with negative groups, which decreased the adsorption by the repulsive electrostatic forces according to the reaction: $\equiv\text{FeOH} \leftrightarrow \equiv\text{Fe-O}^- + \text{H}^+$; such adsorption behavior was also detected by previous researchers.^{10,18} The Sb(III) mainly exists as H_3SbO_3 and $\text{Sb}(\text{OH})_3$ at pHs between 2.0 and 10.4 and as H_2SbO_3^- and $\text{Sb}(\text{OH})_4^-$ at pHs above 10.4. Meanwhile, Sb(V) mainly exists as H_2SbO_4^- and

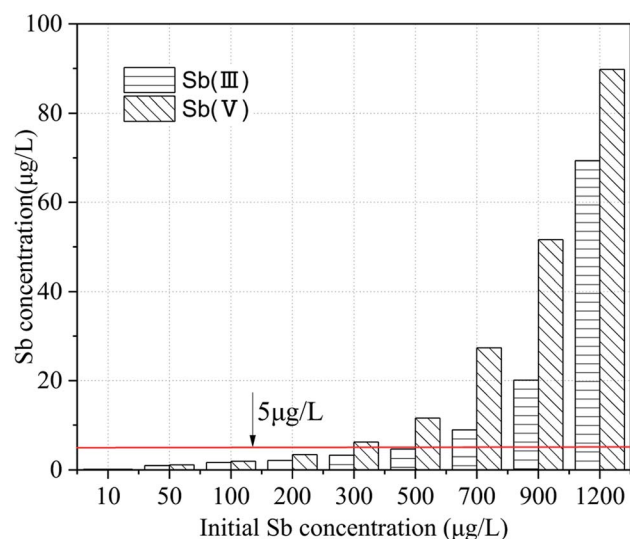


Fig. 6 The remaining antimony concentration after the modified iron powders were used as an adsorbent for low-level antimony removal ($t = 25 \pm 1$ °C, adsorbent dose: 0.25 g L^{-1} , pH = 5.0 ± 0.2 ; total solution volume: 100 mL ; reaction time: 360 min).



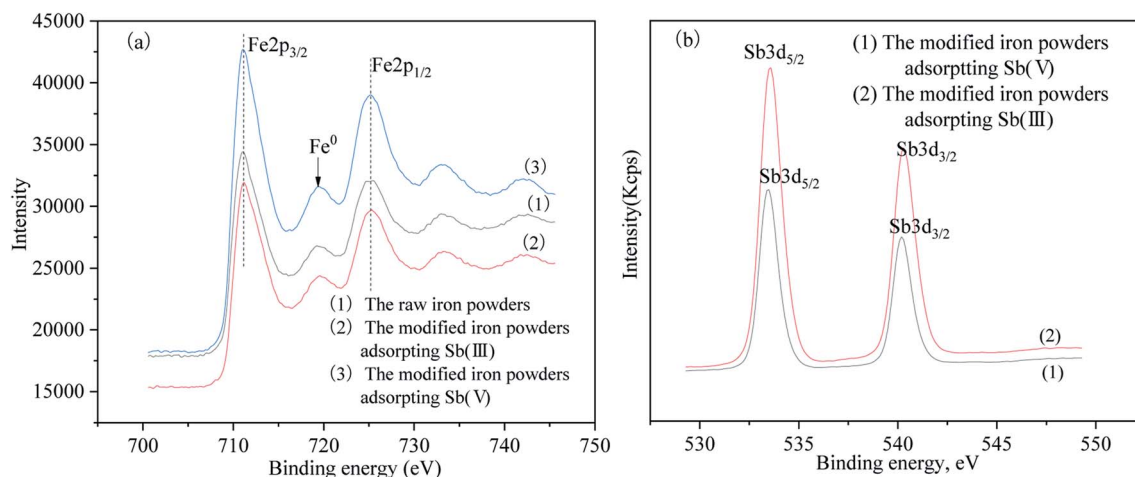


Fig. 7 The XPS spectral analysis of (a) Fe 2p and (b) Sb 3d.

Table 3 The peak table data of the XPS analysis

Name	Start BE	Peak BE	End BE	Height (CPS)	FWHM (eV)	Area (P) (CPS.eV)	Area (N)	Atomic%
Fe 2p	738.29	711.09	706.19	22 046.07	3.73	188 577.8	0.34	23.28
Fe 2p	737.89	711.16	706.39	14 555.14	3.58	111 154.1	0.20	17.07
Fe 2p	737.39	711.03	705.89	14 493.87	3.44	100 607.4	0.18	13.29
Sb 3d	550.01	540.19	537.71	47 719.02	1.26	115 451.3	0.10	6.6
Sb 3d	549.61	540.08	537.71	28 863.87	1.12	63 074.44	0.05	4.49

$\text{Sb}(\text{OH})_6^-$ when the pH is above 2.7.⁷ The more negatively charged surfaces increased the repulsive forces and inhibited the adsorption of the anionic H_2SbO_3^- and $\text{Sb}(\text{OH})_4^-$. The decreased adsorption capacity might be attributed to the electrostatic repulsion.

3.5 Application of the modified for adsorption of low-level antimony

The Zijiang river basin lies in the Hunan province, China and provides drinking water to the people in the cities along the river basin. The Lengshuijiang city called 'the Antimony City of the world' is just located in the upper reaches of the Zijiang river and produces more than 30% of the total antimony production in the world. The concentration of antimony in the river water was between 11 and 14 $\mu\text{g L}^{-1}$ on sunny days and was always more than 10 times the concentration on rainy days, which resulted from the rain washing the antimony down the river. The concentration of antimony during the monitoring period exceeded the concentration 5 $\mu\text{g L}^{-1}$ specified in the specification of the "Standards for drinking water quality" (GB5749-2015) of China. The application of the modified iron powders was used for the advanced treatment to remove the antimony from the drinking water. A simulated raw water with different initial antimony concentrations was prepared and the atomic fluorescence spectrometry method was adopted to determine the low-level antimony concentration. The treatment results are presented in Fig. 6. The modified iron powders can reduce the

antimony concentration to below 5 $\mu\text{g L}^{-1}$ when the $\text{Sb}(\text{III})$ and $\text{Sb}(\text{V})$ was no more than 500 $\mu\text{g L}^{-1}$ and 300 $\mu\text{g L}^{-1}$, respectively, which implied that the modified iron powders can be used for the treatment of drinking water with a low-level antimony content. Previous researchers used iron-based oxy-hydroxides as adsorbents to treat groundwater containing Sb to meet the requirements of the drinking water regulations. The higher efficiency of the validated FeOOH was confirmed by rapid small-scale column tests, because an adsorption capacity of 3 mg

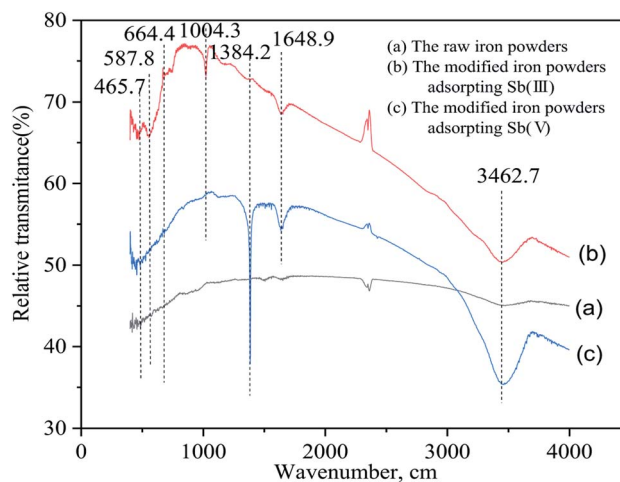


Fig. 8 The FT-IR spectral analysis of the different materials.



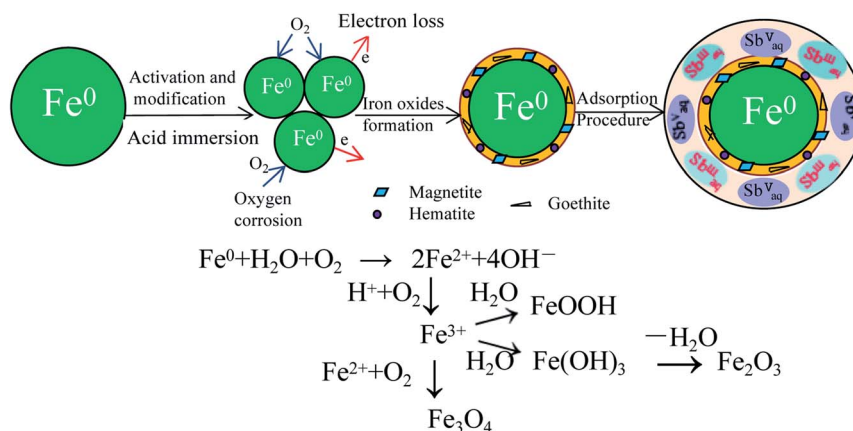


Fig. 9 A probable schematic process diagram for the adsorption process.

$\text{Sb}(\text{III})$ g^{-1} was determined at a breakthrough concentration of $5 \mu\text{g L}^{-1}$. However, it completely failed to achieve $\text{Sb}(\text{V})$ concentrations below $5 \mu\text{g L}^{-1}$ even at the beginning of the column experiments.¹¹ In view of this, the researchers developed a new amorphous $\text{Fe}_3\text{O}_4/\text{FeOOH}$ nanocomposite to treat drinking water containing $\text{Sb}(\text{V})$. The addition of the reducing agent such as Fe_3O_4 results in the improvement of the $\text{Sb}(\text{V})$ uptake capacity and the intermediate reduction of $\text{Sb}(\text{V})$ to $\text{Sb}(\text{III})$ followed by $\text{Sb}(\text{III})$ adsorption onto the FeOOH is the possible mechanism which explains the experimental findings.¹⁹ Compared with the synthesized iron oxide based adsorbents, the preparation of the adsorptive material in the present study has a cost advantage.

3.6 Adsorption mechanism

3.6.1 XPS analysis. The Fe 2p and Sb 3d transmittance spectra of the raw iron powder, the activated and modified iron powders after $\text{Sb}(\text{III})$ or $\text{Sb}(\text{V})$ adsorption at $\text{pH } 5.0 \pm 0.2$ are presented in Fig. 7(a) and (b). According to the results in Fig. 7(a), Fe^0 existed in the activated and modified iron powders at the binding energy peak of 718 eV.¹³ Simultaneously, a certain amount of the iron oxides were also displayed by the binding energy peaks of Fe 2p_{3/2} (711.0 eV) and Fe 2p_{1/2} (725.19 eV). The Fe 2p_{3/2} and the Fe 2p_{1/2} energy peaks still were observed at the surface of the raw iron powder, mainly due to oxidization by air.^{9,13} After the activation and modification treatment, the surface of the zero-valent iron powders, such as hematite, goethite and magnetite, was oxidized to the $\text{Fe}(\text{III})$ oxidation state, according to the results of the SEM, XRD and the XPS Fe 2p analyses.

The Sb 3d_{3/2} peaks were found at the 540.19 eV, which appeared in both the modified iron powders after the adsorption of $\text{Sb}(\text{III})$ and $\text{Sb}(\text{V})$.¹³ According to results in Table 3, the surface contents of $\text{Sb}(\text{III})$ and $\text{Sb}(\text{V})$ were 6.6% and 4.49%, respectively. Because of the similar binding energies, the $\text{Sb}(\text{III})$ and $\text{Sb}(\text{V})$ oxidation states cannot be distinguished. Furthermore, the combination of $\text{Sb}(\text{III})$ and $\text{Sb}(\text{V})$ adsorbed on the surface of the iron oxides cannot be distinguished because of the lack of reported binding energy references in the literature to correlate this. Nevertheless, the Sb 3d_{3/2} binding energy

peaks demonstrated that $\text{Sb}(\text{III})$ and $\text{Sb}(\text{V})$ in the solution were both chemically adsorbed onto the surface of the modified iron powders. Moreover, the intensity of the Sb 3d_{3/2} peak for the modified iron powder adsorbed $\text{Sb}(\text{III})$ was stronger than the powders which adsorbed $\text{Sb}(\text{V})$, which was in agreement with the higher binding affinity of $\text{Sb}(\text{III})$ to the iron oxides on the surface of the modified iron powders than $\text{Sb}(\text{V})$ and was consistent with the experimental results of the adsorption isotherm.^{9,13}

3.6.2 FT-IR spectroscopy analyses. The FT-IR spectroscopy analyses of the raw iron powders and the modified iron powder adsorbed $\text{Sb}(\text{III})$ and $\text{Sb}(\text{V})$ are presented in Fig. 8. The broad spectroscopy peak located at about 3462.7 cm^{-1} could be attributed to the O–H bonds stretching resulting from the free water; the bands at 1648.9 cm^{-1} and 1384 cm^{-1} may be ascribed to the C–H bonds stretching in the residual acetic acid when the iron powders were modified and the 1004.3 cm^{-1} peak could be attributed to the C–O in the residual acetic acid or CO_3^{2-} species.^{20,21} The spectroscopy peak at 664.4 cm^{-1} was likely to result from the Fe–O–H bands and the peaks at 465.7 cm^{-1} and 587.8 cm^{-1} could be attributed to the Fe–O–Sb bands, which demonstrated that the $\text{Sb}(\text{III})$ or $\text{Sb}(\text{V})$ in solution was adsorbed by the iron oxides on the surface of the modified iron powders.^{9,13}

3.6.3 Schematic process diagram analyses. The images in Fig. 2 showed that the surface of the iron powders changed greatly after activation and modification and $\gamma\text{-Fe}_2\text{O}_3$, $\gamma\text{-FeOOH}$ and Fe_3O_4 were obtained. Based on the images shown in Fig. 2, the schematic diagram for the adsorption process of the $\text{Sb}(\text{III})$ and $\text{Sb}(\text{V})$ by the modified iron powders is presented in Fig. 9. As described previously, the enhanced $\text{Sb}(\text{III})$ and $\text{Sb}(\text{V})$ removal rates were assigned to the mechanical activation and acid modification induced improvement in the physicochemical property of superficial corrosion. The mechanical activation and acid modification accelerated the loss of the electron from the iron atom and the oxygen corrosion of the surface. The probable reaction paths for iron corrosion and iron oxide formation are presented in Fig. 9. Under the action of H_2O and O_2 , the surface Fe^0 transformed into Fe^{2+} and Fe^{3+} was subsequently obtained. Then, part of Fe^{3+} was converted into FeOOH



and amorphous $\text{Fe}(\text{OH})_3$; some Fe^{3+} changed into Fe_3O_4 with the use of Fe^{2+} and O_2 . The removal of $\text{Sb}(\text{III})$ and $\text{Sb}(\text{V})$ in the solution can not only be attributed to the adsorption by the iron, but also to the substitution of the hydrogen atom on the band of O–H by $\text{Sb}(\text{III})$ and $\text{Sb}(\text{V})$ and the band Fe–O–Sb formed, which was determined in the XPS and FT-IR analyses.

4 Conclusions

In summary, an adsorbent was obtained using zero-valent iron powders by ball-milling and acid modification. Such iron oxides as Fe_3O_4 , $\gamma\text{-Fe}_2\text{O}_3$ and $\gamma\text{-FeOOH}$ were obtained in the corrosion layer on the surface of the zero-valent iron powders. The modified iron powders were adopted to remove $\text{Sb}(\text{III})$ and $\text{Sb}(\text{V})$ in solution. The study showed that the experimental data fitted the Langmuir model and the pseudo-first-order kinetic model better and the adsorption process was monolayer and chemically controlled at $\text{pH } 5.0 \pm 0.2$. The XPS and FT-IR analysis showed that the O–Sb bond arose during the adsorption process. The schematic process diagram was completed to show the probable mechanism. The ball-milling and acid modification increased the adsorption capacity for $\text{Sb}(\text{III})$ and $\text{Sb}(\text{V})$ from 12.93 mg g^{-1} and 5.47 mg g^{-1} to 17.96 mg g^{-1} and 10.58 mg g^{-1} , respectively. Although the adsorption capacities were relatively lower than those reported for pure iron oxides, the material availability contributed to the benefits of its application.

Conflicts of interest

There are no conflicts to declare.

Acknowledgements

This work was financially supported by the Natural Science Foundation of Hunan Province (2017JJ2020), the Outstanding Youth Project of the Department of Education of Hunan Province (16B049), the Science and Technology Projects of Yiyang (2015JZ26), the Science and Technology Program of Education Department of Hunan Province (16C0303) and the Science and Technology Program of Education Department of Hunan Province (18C0840).

Notes and references

- 1 C. Shan, Z. Ma and M. Tong, *J. Hazard. Mater.*, 2014, **268**, 229–236.

- 2 J. Xi, M. He, K. Wang and G. Zhang, *J. Geochem. Explor.*, 2013, **132**, 201–208.
- 3 J. Li, B. Zheng, Y. He, Y. Zhou, X. Chen, S. Ruan, Y. Yang, C. Dai and L. Tang, *Ecotoxicol. Environ. Saf.*, 2018, **156**, 125–134.
- 4 X. Li, X. Dou and J. Li, *J. Environ. Sci.*, 2012, **24**, 1197–1203.
- 5 J. Xi, M. He and C. Lin, *Microchem. J.*, 2011, **97**, 85–91.
- 6 V. J. Ritchie, A. G. Ilgen, S. H. Mueller, T. P. Trainor and R. J. Goldfarb, *Chem. Geol.*, 2013, **335**, 172–188.
- 7 X. Y. Guo, Y. T. Xin, H. Wang and Q. H. Tian, *Trans. Nonferrous Met. Soc. China*, 2015, **25**, 4175–4182.
- 8 G. Ungureanu, S. Santos, B. Rui and C. Botelho, *J. Environ. Manage.*, 2015, **151**, 326–342.
- 9 Z. Qi, T. P. Joshi, R. Liu, H. Liu and J. Qu, *J. Hazard. Mater.*, 2017, **329**, 193–204.
- 10 R. Liu, W. Xu, Z. He, H. Lan, H. Liu, J. Qu and T. Prasai, *Chemosphere*, 2015, **138**, 616–624.
- 11 K. Simeonidis, V. Papadopoulou, S. Tresintsi, E. Kokkinos, I. A. Katsoyiannis, A. I. Zouboulis and M. Mitrakas, *Sustainability*, 2017, **9**, 238–249.
- 12 P. Fan, Y. Sun, J. Qiao, I. Lo and X. Guan, *J. Hazard. Mater.*, 2017, **343**, 266–275.
- 13 X. Zhao, X. Dou, M. Dinesh, P. U. Charles, S. O. Yong and J. Xin, *Chem. Eng. J.*, 2014, **247**, 250–257.
- 14 X. Guo, Z. Wu, M. He, X. Meng, X. Jin, N. Qiu and J. Zhang, *J. Hazard. Mater.*, 2014, **276**, 339–345.
- 15 F. Kolbe, H. Weiss, P. Morgenstern, R. Wennrich, W. Lorenz, K. Schurk, H. Stanjek and B. Daus, *J. Colloid Interface Sci.*, 2011, **357**, 460–465.
- 16 Z. Lan, J. Wei, Z. Xuan, F. Li and J. Feng, *Chem. Eng. J.*, 2015, **277**, 378–387.
- 17 X. Wang, M. He, C. Lin, Y. Gao and Z. Lei, *Geochemistry*, 2012, **72**, 41–47.
- 18 B. J. Lafferty, M. Gindervogel, M. Zhu, K. J. T. Livi and D. L. Sparks, *Environ. Sci. Technol.*, 2010, **44**, 8467–8472.
- 19 K. Simeonidis, K. Kalaitzidou, E. Kaprara, G. Mitraka, T. Asimakidou, L. Balcells and M. Mitrakas, *Water*, 2019, **11**.
- 20 Z. Qi, T. P. Joshi, R. Liu, Y. Li, H. Liu and J. Qu, *J. Hazard. Mater.*, 2017, **343**, 36.
- 21 L. R. Braga, A. A. Rosa and A. C. B. Dias, *Anal. Methods*, 2014, **6**, 4029.

